

Supplementary information

Structural Insights of Mechanochemically Amorphised MIL-125-NH₂

Emily V. Shaw,^a Celia Castillo-Blas,^{*a} Timothy Lambden,^a Beatriz de Santos,^b Bethan Turner,^c Giulio I. Lampronti,^a Joonatan E. M. Laulainen,^a Georgina P. Robertson,^{a,d} Ashleigh M. Chester,^a Chumei Ye,^{a,e} Shaoliang Guan,^{a,e} Joshua K. G. Karlsson,^a Valentina Martinez,^f Ivana Brekalo,^f Bahar Karadeniz,^f Silvia Cabrera,^{g,h} Lauren N. McHugh,^c Krunoslav Užarević,^f Jose Alemán,^{b,h} Alberto Fraile,^{b,h} Rachel C. Evans,^a Paul A. Midgley,^a David A. Keen,ⁱ Xavier Moya,^a and Thomas D. Bennett^{*j}

^a Department of Materials Science & Metallurgy, University of Cambridge, 27 Charles Babbage Road, Cambridge, UK. E-mail: cc2078@cam.ac.uk

^b Organic Chemistry Department, Science Faculty, Universidad Autónoma de Madrid, C/ Francisco Tomás y Valiente, 7, 28049, Madrid, Spain.

^c Department of Chemistry, University of Liverpool, Crown Street, Liverpool L69 7ZD, U.K.

^d Diamond Light Source Ltd., Diamond House, Harwell Campus, Didcot, Oxfordshire, UK

^e Maxwell Centre, Cavendish Laboratory, University of Cambridge, J. J. Thomson Avenue, Cambridge, CB3 0HE United Kingdom.

^f Division of Physical Chemistry, Ruđer Bošković Institute, Zagreb, Croatia

^g Inorganic Chemistry Department, Ruđer Bašković Institute, Zagreb, Croatia Madrid, C/Francisco Torrás y Valiente 7, 28049 Madrid, Spain

^h Institute for Advanced Research in Chemical Science (IAdChem), Universidad Autónoma de Madrid, C/Francisco Tomás y Valiente, 7, 28049, Madrid, Spain.

ⁱ ISIS Facility, Rutherford Appleton Laboratory, Harwell Campus, Didcot, Oxfordshire, UK

^j School of Physical and Chemical Sciences, University of Canterbury, Private Bag 4800, Christchurch 8140, New Zealand. E-mail: thomas.bennett@canterbury.ac.nz

Table of Contents

1. Synthetic Methods	2
2. PXRD Characterisation	6
3. Scanning Electron Microscopy	10
4. Total Scattering and Pair Distribution Function Analysis	11
5. X-ray Photoelectron Spectroscopy	18
6. Fourier-Transform Infrared Spectroscopy	20
7. Compositional Analysis	21
8. Applications	23
9. References	26

1. Synthetic Methods

Synthesis of MIL-125-NH₂. 2-aminoterephthalic acid (2.8 g, 15 mmol) was added to a dissolved in a 9:1 solution of DMF (45 mL) and methanol (5 mL) in a 100 mL Teflon tube, and stirred for 10 minutes. On addition of Ti(OⁱPr)₄ (3 mL, 10 mmol) the solution began to gelate into a bright orange gel and left to stand for 10 minutes. The Teflon tube was sealed in an Autoclave and heated at 150 °C for 15 h. The yellow powder was separated and washed using a centrifuge, washing in DMF (3 x 20 mL), ethanol (5 x 20 mL) and acetone (2 x 20 mL). The resultant powder was dried overnight under a dynamic vacuum at 150 °C.

Ball-Milling was carried out on evacuated powder samples. The sample was activated using a dynamic vacuum at 150 °C overnight. To form a_mMIL-125-NH₂, MIL-125-NH₂ (120 mg) was added to a 10 mL stainless steel jar, along with 1 x 10 mm diameter stainless steel ball bearing (4.03 g) at room temperature. The jar was then ball-milled at 30 Hz on a Retsch MM400 mixer mill for 1-, 3-, 7- and 15-minute durations. After milling, the powder was recovered and characterised.

Powder X-ray diffraction (PXRD) data were collected at room temperature using a Bruker D8 diffractometer using Cu K α radiation ($\lambda = 1.5418 \text{ \AA}$) over the scattering angle range $2^\circ < 2\theta < 50^\circ$. Pawley refinements were carried out using TOPAS Academic (V6) software.¹ The unit cell parameters were refined against those previously reported for MIL-125 over the angular range $2^\circ < 2\theta < 50^\circ$.

Thermogravimetric Analysis (TGA) was performed on a TA instruments SDT-Q600, under an air atmosphere, using a heating rate of 10 °C min⁻¹, from room temperature to 800 °C. An isotherm was performed at 100 °C for 10 minutes to ensure complete removal of solvent. Between 5-15 mg of activated sample was used for each measurement.

Fourier-Transformed Infrared Spectroscopy (FT-IR) data were collected on a Bruker Tensor 27. Data were collected in transmission mode between 600 and 4000 cm⁻¹ through the use of an attenuated total reflectance cell. A background was collected and subtracted from all spectra, as well as an atmospheric correction.

Elemental Analysis, CHN combustion analysis, was performed using a CE440 Elemental Analyser, EAI Exeter Analytical Inc. ~2 mg of sample was used for each run to give C, H and N % values.

Scanning Electron Microscopy (SEM) was performed using a FEI Nova NanoSEM operated at 5 keV for imaging using secondary electrons. Samples were prepared for SEM by securing to aluminium SEM pin stubs using carbon tape. Samples were coated in gold using an Emtech K575 sputter coater prior to imaging to prevent charging.

Scanning Electron Diffraction (SED) data was acquired on a TF Spectra 300 operated at 300 keV with a probe diameter of ca. 4 nm and a convergence angle of ca. 0.6 mrad. The current was 2 pA, and the data was acquired on a Merlin Medipix3 with a frame time of 1 ms, leading to an electron dose of ca. 10 e⁻/Å². Data were collected at a camera length of 91 mm, and a C2 aperture of 30 μm . Diffraction and real-space calibration was performed using an AuPd grid. SED data were processed using pyxem.²

Synchrotron *In-Situ* Ball-Milling PXRD experiments were performed at the Deutsches Elektronen synchrotron, Hamburg, at PETRA III beamline P02.1. The beamline was equipped

with a Varex XRD4343CT detector and modified IST-636 vibratory ball mill. Beam alignment and calibration was performed using a Si standard in a poly(methyl methacrylate) PMMA milling jar. For the amorphisation of MIL-125-NH₂, 200 mg evacuated MIL-125-NH₂ was added to a 10 mL PMMA ball mill jar with a 10 mm stainless steel ball and milled for 30 minutes at 30 Hz, with the PMMA background contribution removed during data processing. The beam size was ca. 1 x 1 mm² with $\lambda = 0.20735 \pm 0.00001 \text{ \AA}$ (59.79321 \pm 0.00159 keV). Time-resolved diffractograms were generated by MATLAB R2023a using the MATLAB scripts developed by Dr Stipe Lukin.

In-Situ PXRD Sequential Refinements The one-dimensional PXRD traces were extracted from the collected two-dimensional images through integration with the DAWN Science package. The crystalline material was first fitted *via* Rietveld refinement with data collected on laboratory PXRD, using TOPAS Academic (V6) software, to confirm the unit cell parameters of the material.¹ The scattering of the amorphous material was fitted as a single Gaussian peak. The fixed experimental background was defined through fitting of the 10 second milling sample with the refined crystalline model, the empty jar background and a refined background function, to account for the 'non-ideal' nature of an experimental sample. Sequential refinements were performed, with a convergence criterion of 0.001 and a maximum number of iterations of 10000. Peak splitting, as a result of the random distribution of powder inside the ball-milled jar, was accounted for by the crystalline model being introduced twice, with a two modified Thompson-Cox-Hastings pseudo- Voigt functions (TCHZ), peak shape functions (with fixed parameters as refined on the Si standard), and independent scale parameters. The TCHZ function was defined by Lampronti *et al.*^{3,4} The methodology utilised for this sequential refinement follows the methodology and underpinning theory described by Ye *et al.*⁵

X-ray Total Scattering and Pair Distribution Function Analysis data were collected at the Deutsches Elektronen synchrotron, Hamburg, at PETRA III beamline P02.1. (beam time allocation I20230031EC) ($\lambda = 0.20734 \text{ \AA}$). A small amount of finely ground sample was loaded into a Kapton capillary (inner diameter of 0.5 mm) to a height of 3 cm. Capillaries were sealed and mounted onto the instrument. Data were collected at room temperature for each sample, an empty capillary and the blank instrument over the region $\sim 0.3 < Q < \sim 26 \text{ \AA}^{-1}$. The total scattering data were processed to account for absorption corrections and various scattering corrections (background scattering, multiple scattering, container scattering and Compton scattering) in a Q range of $0.3\text{--}20 \text{ \AA}^{-1}$. Subsequent Fourier transformations of the processed total scattering data resulted in a real-space PDF $G(r)$ for each material. In this work, we use the $D(r)$ form of the PDF to accentuate high r correlations. All processing of the total scattering data was performed using GudRunX following well-documented procedures.⁶⁻⁸

Published structural models were refined against PDF data using PDFGui, producing partial PDFs for each correlation.⁹ Values were initially set and fixed at $r_{\text{cut}} = 5.75 \text{ \AA}$ and $Q_{\text{broad}} = 0.0001$. $Q_{\text{damp}} = 0.08$, data scale factor = 0.5 and model scale factor = 1.0 were utilised as starting values and then refined. Refinements were done in the range $0.5 < r < 15 \text{ \AA}$, with $Q_{\text{max}} = 23 \text{ \AA}^{-1}$. Thermal parameters were refined isotropically, defined initially as 0.0025 \AA^2 . Atomic positions were refined within appropriate symmetry constraints, defined by the space group, with limited variation observed from their starting positions. Structural models for the secondary building units (SBUs) were obtained from published crystalline models, with the model unit cell expanded to remove SBU-SBU correlations. Refinements were done in the range $0.5 < r < 12.5 \text{ \AA}$, with $Q_{\text{max}} = 15 \text{ \AA}^{-1}$

Principal Component Analysis (PCA) were carried out on the $D(r)$ functions with Origin v2019 graphing software.¹⁰ PCA is a dimensionality reduction technique, representing them in order of explained variance. PCA was applied to the set of five $D(r)$ functions, defined by their

time ball-milled, 0, 1, 3, 7 and 15 minutes. From these, 3 principal components (PCs) were extracted that were deemed statistically significant.

X-ray Photoelectron Spectroscopy (XPS) Analysis was performed using a Thermo NEXSA G2 XPS fitted with a monochromated Al $K\alpha$ X-ray source (1486.7 eV), a spherical sector analyser and 3 multichannel resistive plate, 128 channel delay line detectors. All data were recorded at 19.2W and an X-ray beam size of 400 x 200 μm . Survey scans were recorded at a pass energy of 200 eV. Electronic charge neutralization was achieved using an ion source (Thermo Scientific FG-03). Ion gun current = 150 μA . Ion gun voltage = 40 V. All sample data were recorded at a pressure below 10^{-8} Torr and a room temperature of 294 K. Data were analysed using CasaXPS v2.3.26rev1.0N.

Photocatalytic Activity Testing: Benzylamine (10.8 mg, 0.1 mmol), 1 mg of material in 1 mL of dry acetonitrile was irradiated at the indicated wavelength (450 or 520 nm) for the corresponding time. The yields were determined by ^1H NMR analysis using 1,3,5-trimethoxybenzene as the quantitative standard.

The reactions were run in a custom-made temperature-controlled system. The reaction mixture was kept at room temperature by passing coolant through the metallic system employing a recirculating chiller, and the irradiation was achieved with a single 22 mW blue LED (450 nm) or 22 mW green LED (520 nm) located 1 cm beneath the base of the vial.

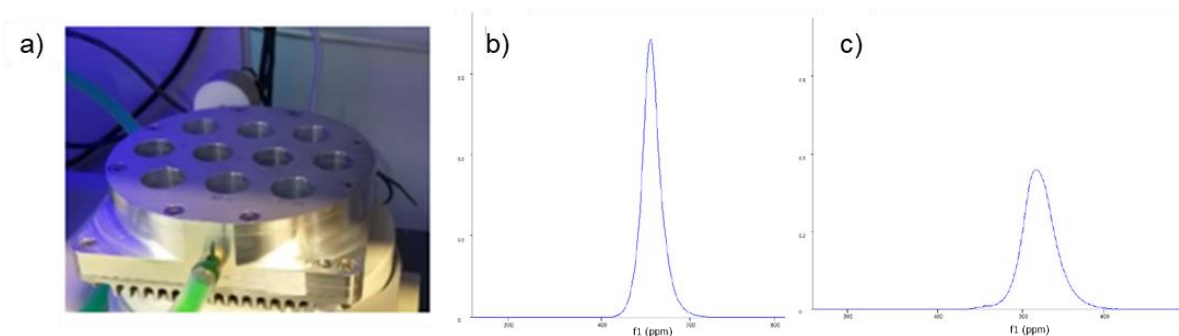


Figure S1: a) Photograph of the custom-made photoreactor system. Emission spectrum of b) 18 mW purple LED (420 nm), c) 22 mW blue LED (450 nm), d) 22 mW green LED (520 nm) and e) 40 mW white LED.

Nuclear Magnetic Resonance (NMR) spectra were acquired on a BRUKER AVANCE spectrometer running at 300 MHz for ^1H , and are internally referenced to the residual CDCl_3 signal: δ 7.26 ppm for ^1H NMR. Data for ^1H NMR are reported as follows: chemical shift (δ ppm), multiplicity, coupling constant J (Hz) and integration.

Gas sorption, gas uptake measurements and adsorption analysis of CO_2 up to 0.032 p/p $^\circ$ at 273 K were performed on a Micrometric 3-Flex 3500 Gas Sorption Analyser. Samples of ca. 90 mg were degassed in situ with nitrogen by heating to 383 K at a rate of 10 K per minute under vacuum for 16 hours. Adsorption and desorption Isotherms were produced, providing values for the maximum uptake and trends in adsorption/desorption. Analysis was performed with Micromeritics Flex Version 6.02 software. The gas uptake measurements and adsorption analysis of N_2 up to 1 p/p $^\circ$ at 77 K were performed on a Micrometric 3-Flex 3500 Gas Sorption Analyser. Samples of ca. 90 mg were degassed in situ with nitrogen by heating to 373 K at a rate of 10 K per minute under vacuum for 15 hours. Adsorption and desorption isotherms were produced, providing values for the maximum uptake and trends in adsorption/desorption. Analysis was performed with Micromeritics Flex Version 6.02 software.

Diffuse Reflectance UV-Vis spectroscopy measurements were carried out using a Perkin Elmer Lambda 750 spectrophotometer equipped with a Labsphere 60 mm RSA ASSY integrating sphere. Samples were measured in a powder sample holder with a fused quartz disc. Reflectance spectra were transformed using the Kubelka-Munk transformation and band gap energies were determined from a modified Tauc equation, $(F(R)h\nu)^{1/n} = A(h\nu - E_g)$, $F(R) = k/s = (1-R)^2/2R$, where $F(R)$ is the ratio between absorption coefficient (k) and scattering coefficient (s), R is the % reflectance and $h\nu$ is the energy.¹¹ n is the Tauc exponent, and was taken as 1/2, assuming a direct transition.

Whilst literature states that MIL-125-NH₂ undergoes an indirect transition, the values extracted from Tauc plots utilising both the direct ($n=1/2$) and indirect ($n=2$) exponent are similar in value, with the true band gap energy often lying between the two.¹² Because of this, the transition was assumed to be direct, allowing for comparison with the literature, which also commonly makes this assumption.^{13,14}

2. PXRD Characterisation

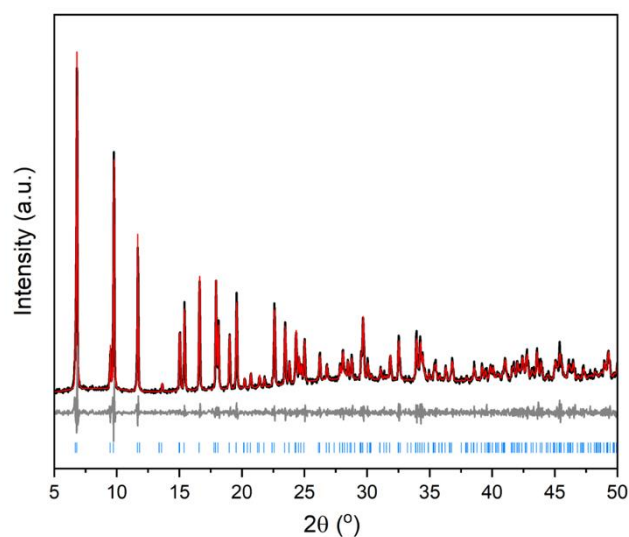


Figure S2: Pawley refinement of MIL-125-NH₂. Experimental data (black), calculated diffraction pattern (red), difference difference the between experimental and calculated data (grey) and symmetry-allowed reflections (blue). Symmetry allowed reflections were calculated from the reported crystallographic information file.¹⁵ Wavelength $\lambda = 1.5418 \text{ \AA}$.

Table S1: Crystallographic data from Pawley refinement of MIL-125-NH₂, literature data from MIL-125.¹⁵

$R_{WP} = 10.373\%$	EXPERIMENTAL LATTICE PARAMETERS	LITERATURE ¹⁵
MIL-125-NH₂	$a, b = 18.681(1) \text{ \AA}$	$a, b = 18.6543(1) \text{ \AA}$
	$c = 18.142(1) \text{ \AA}$	$c = 18.1444(1) \text{ \AA}$
	$\alpha = \beta = \gamma = 90^\circ$	$\alpha = \beta = \gamma = 90^\circ$
	Space Group = $I4/mmm$	Space Group = $I4/mmm$
	$V = 6331.2(1) \text{ \AA}^3$	$V = 6313.9(1) \text{ \AA}^3$

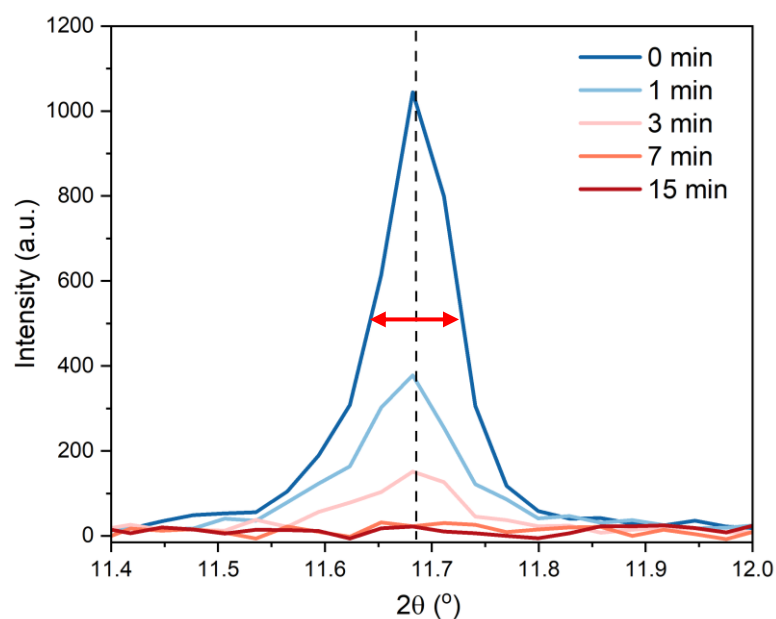


Figure S3: Cropped PXRD data showing the change in the area of the [112]/[211] Bragg peak. The FWHM and centre of the crystalline material (0 min) is shown by the red arrow and dashed line respectively.

Table S2: PXRD peak analysis data for the overlapped (112) and (211) Bragg peaks for samples ball-milled for varying lengths of time. Beyond 3 minutes, no peak was discernable. Peaks were fitted with a Gaussian model using Fityk software.¹⁶

	<i>FWHM / °</i>	<i>PEAK AREA / a.u.</i>	<i>CENTRE / °</i>
<i>0 min</i>	<i>0.11</i>	<i>99.53</i>	<i>11.7</i>
<i>1 min</i>	<i>0.15</i>	<i>46.61</i>	<i>11.67</i>
<i>3 min</i>	<i>0.16</i>	<i>19.92</i>	<i>11.67</i>

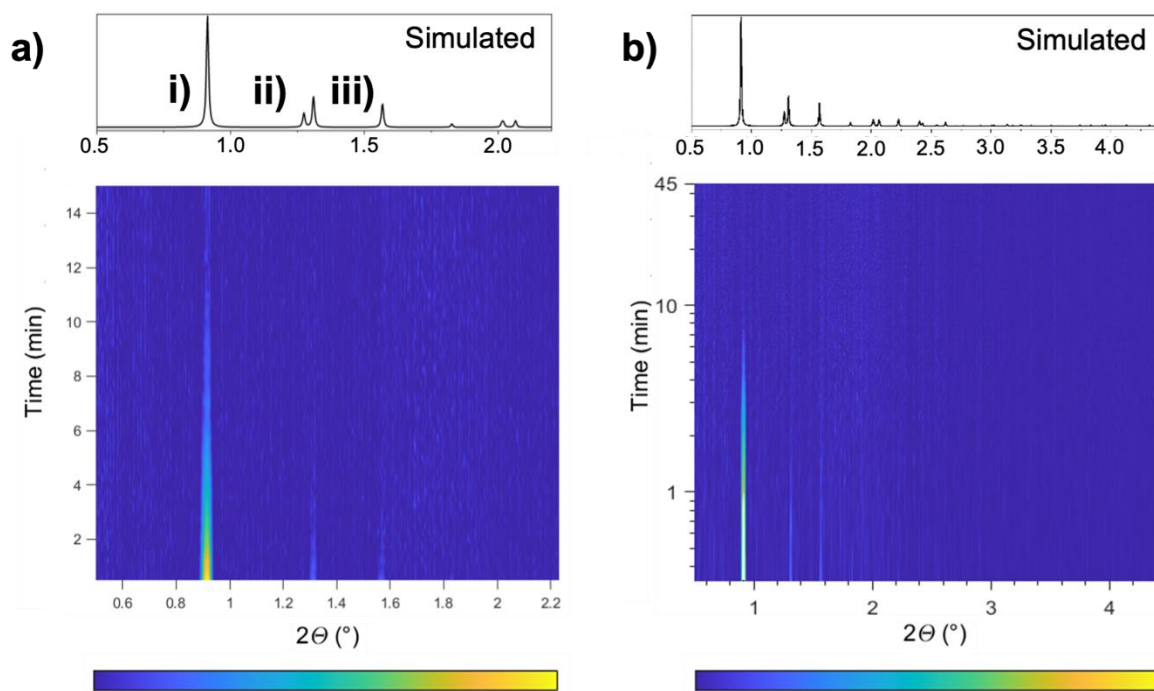


Figure S4: *In-situ* powder X-ray diffraction patterns of MIL-125-NH₂ tracking peak intensity with respect to time ball-milled for a) 15 minutes and b) 45 minutes. The observable peaks were assigned to Bragg peaks i) (110), (101) ii) (200), (002) and iii) (211), (112). The insets display simulated PXRD spectra corresponding to the peaks observed. Wavelength $\lambda = 0.20735 \text{ \AA}$.

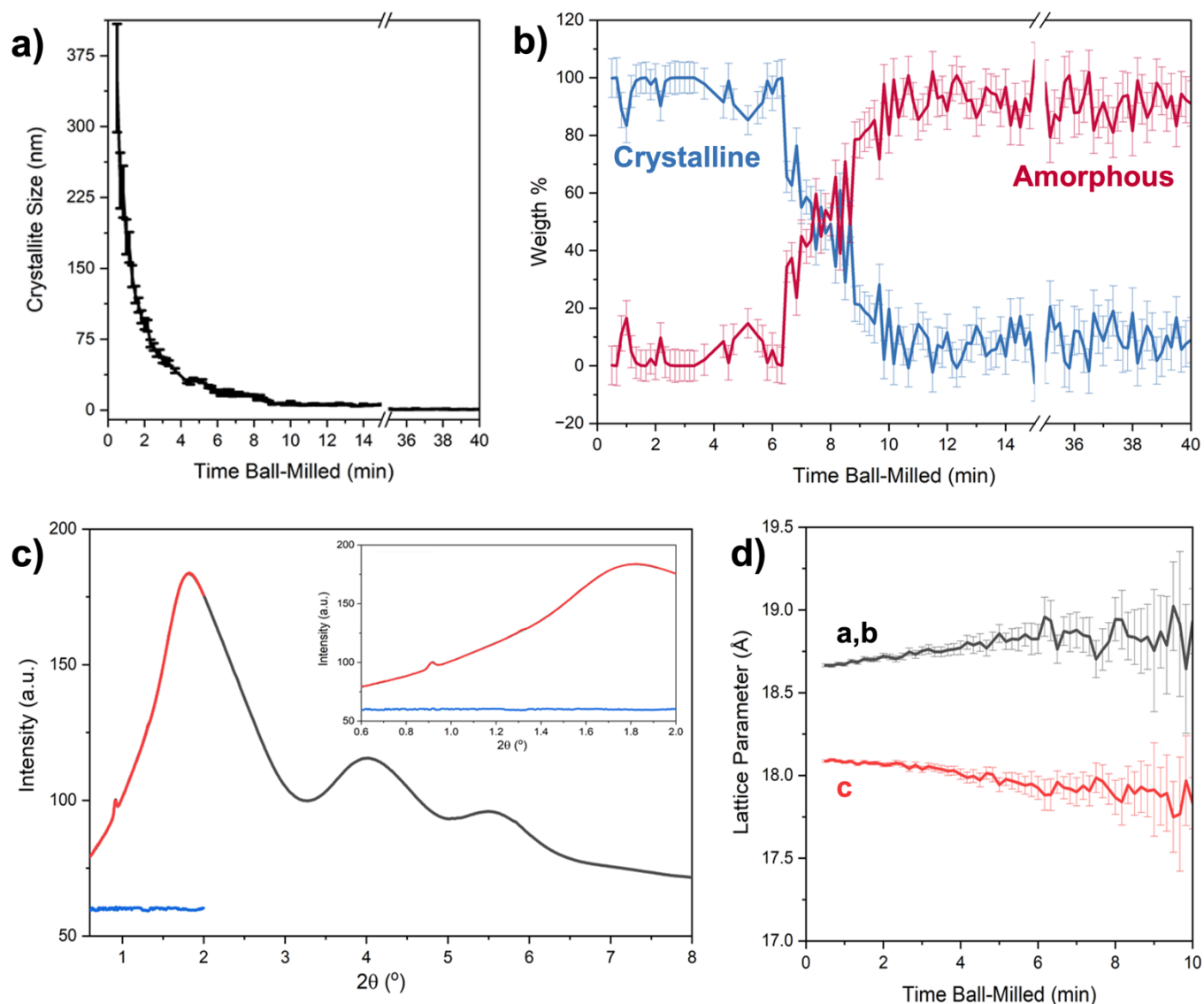


Figure S5: a) Exemplar Rietveld refinement for the diffraction pattern collected at 2 minutes of ball milling, showing the calculated (red), experimental (black) and difference (blue) patterns. The refinement strategy has been previously reported (Supplementary Information in Ye *et al.*, 2024).⁵ Data and input file for sequential refinement are supplied in the supplementary material. b) unit cell parameters extracted from sequential refinement of the *in-situ* ball-milling data showing how the a/b (black) and c (red) lattice parameters vary with time. c) Scherrer crystallite size and d) weight percent quantification for crystalline (blue) and amorphous (red) phases. The crystallite size and phase quantification were run with restrictions on the unit cell parameters, to reduce errors at high milling times. Error bars represent estimated standard deviations. Wavelength $\lambda = 0.20735 \text{ \AA}$.

3. Scanning Electron Microscopy

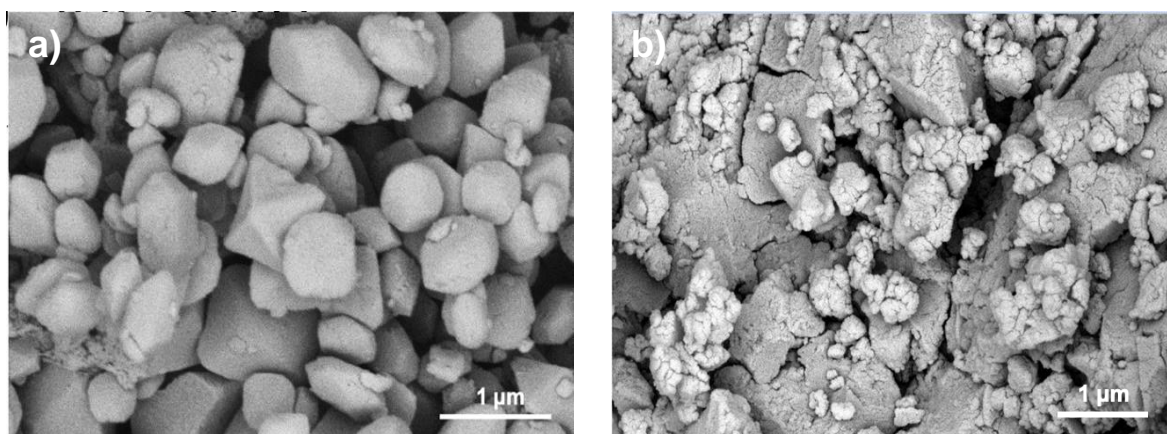


Figure S6: Scanning electron microscopy images of a) MIL-125-NH₂ and b) amMIL-125-NH₂.

4. Total Scattering and Pair Distribution Function Analysis

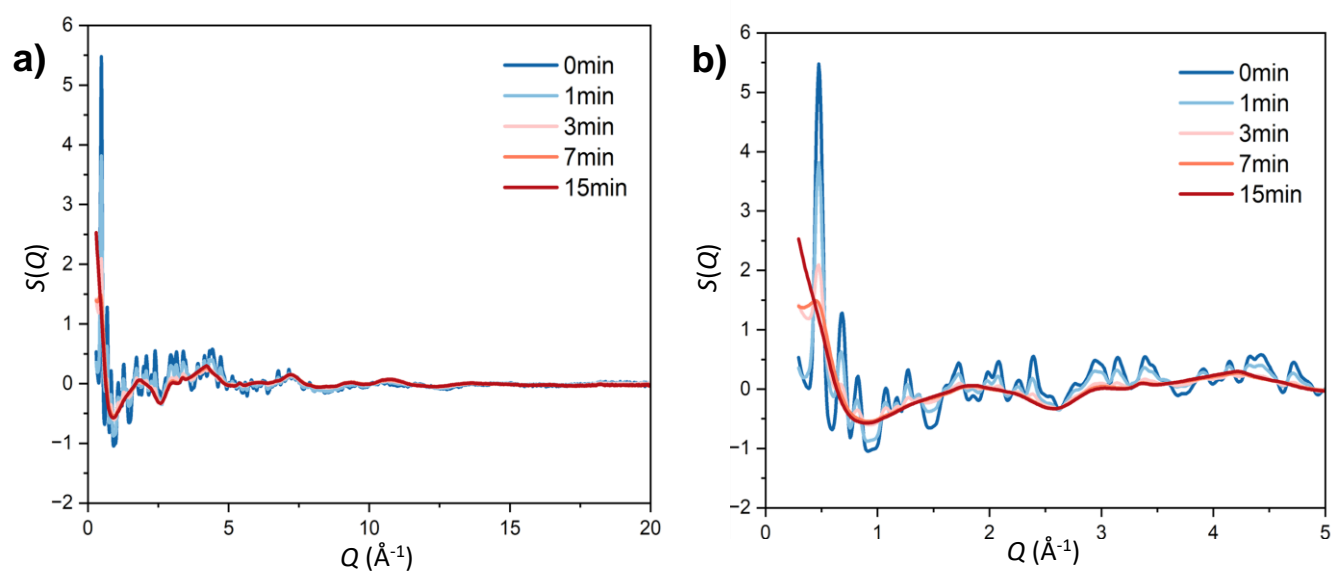


Figure S7: X-ray total scattering structure factors, $S(Q)$, for the MIL-125-NH₂ materials. Key shows duration of ball milling in minutes. a) Full spectra, b) Low-Q region.

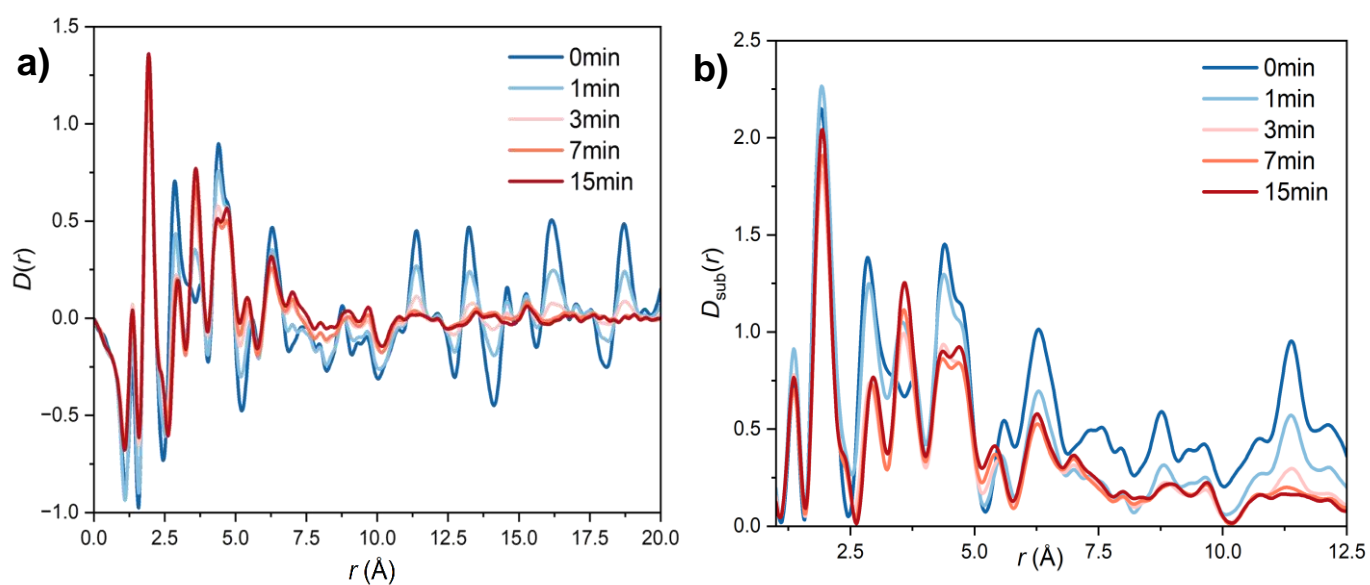


Figure S8: a) Pair distribution functions for the MIL-125-NH₂ materials. b) Baseline subtracted pair distribution functions of the ball-milled materials, baseline was removed using Fityk software.¹⁶

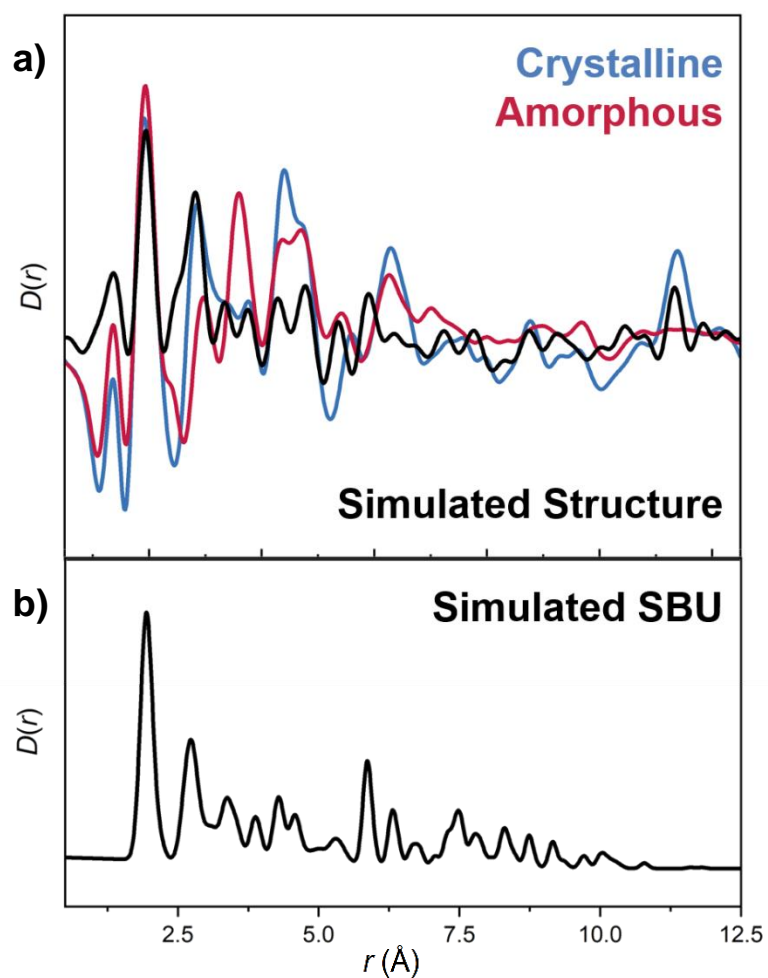


Figure S9: a) Experimental MIL-125-NH₂ (blue), experimental a_mMIL-125-NH₂ (red) and calculated MIL-125-NH₂ (black) pair distribution functions. b) Simulated pair distribution function of the secondary building unit. Simulated spectra do not contain hydrogen based contributions.

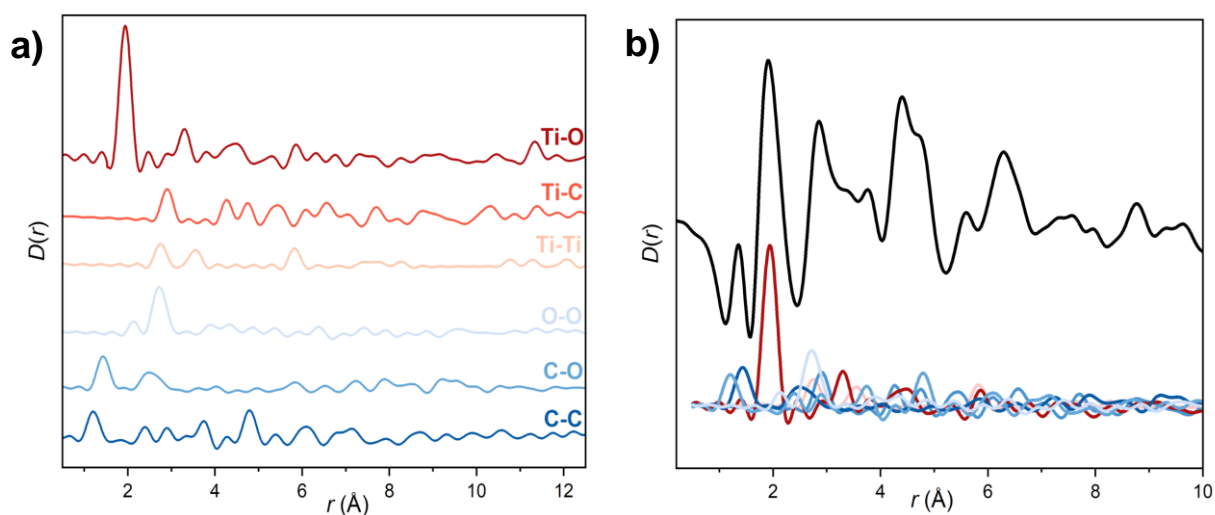


Figure S10: a) Partial pair distribution functions calculated from the crystalline structure of MIL-125-NH₂, partials are offset for clarity. (b) Partial pair distribution functions contribution to the low- r region of the experimental $D(r)$ for MIL-125-NH₂ (black, offset from partials for clarity).

Table S3: Key contributions to each marked PDF peak in Fig. 3a.

PEAKS		CONTRIBUTIONS		
LABEL	PEAK POSITION	C-BASED	SBU	CROSS-LINKER
A	1.36	C-C	-	-
B	1.97	-	O-Ti, O-O	-
C	2.83	Ti-C, C-O	Ti-Ti	-
D	3.39	-	O-Ti	-
E	3.81	C-O, C-C	Ti-Ti, O-Ti, O-O	-
F	4.35	C-Ti, C-O	O-O, O-Ti	-
G	4.79	C-Ti, C-O, C-C	O-O, O-Ti	-
H	5.58	C-Ti, C-O, C-C	O-O, O-Ti, Ti-Ti	-
J	6.29	C-Ti, C-O, C-C	O-O, O-Ti	-
K	7.65	-	Ti-Ti, O-O, O-Ti	O-O
L	8.75	-	Ti-Ti, O-O, O-Ti	Ti-O
M	9.47	-	-	Ti-O, O-O
N	10.46	-	-	Ti-Ti
O	11.37	-	O-O	Ti-Ti, O-O, O-Ti
P	12.12	-	-	Ti-Ti

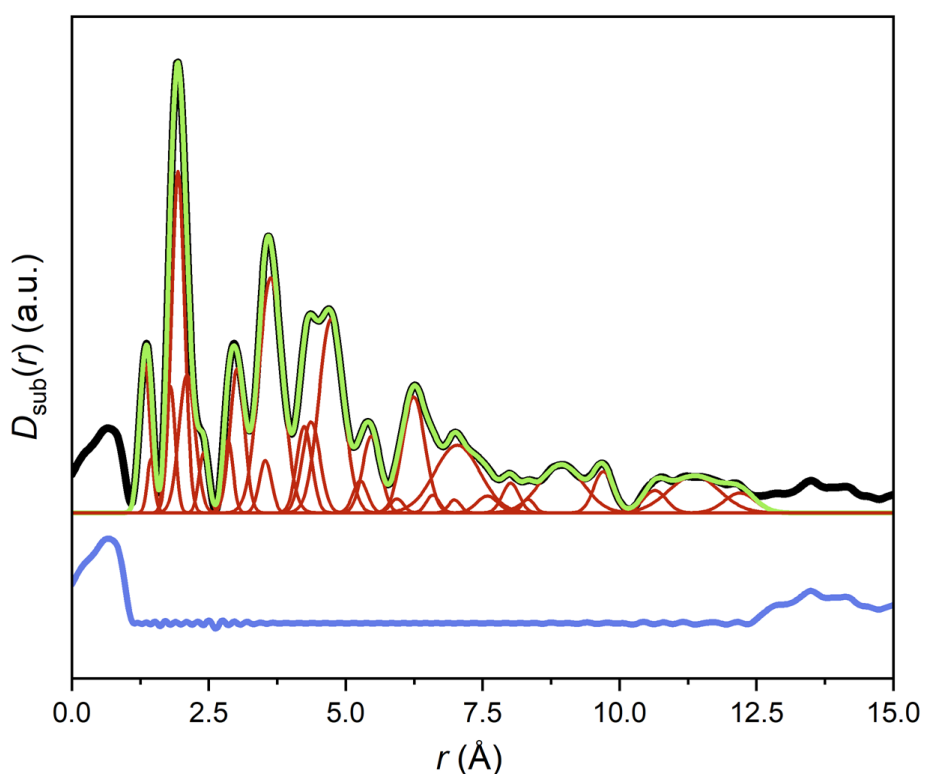


Figure S11: Example of fitting of the background subtracted PDF of $a_m\text{MIL-125-NH}_2$ with the peak areas and positions extracted, showing experimental PDF with background subtracted (black), calculated pattern (green), difference pattern (blue) and the individual contributions (red).

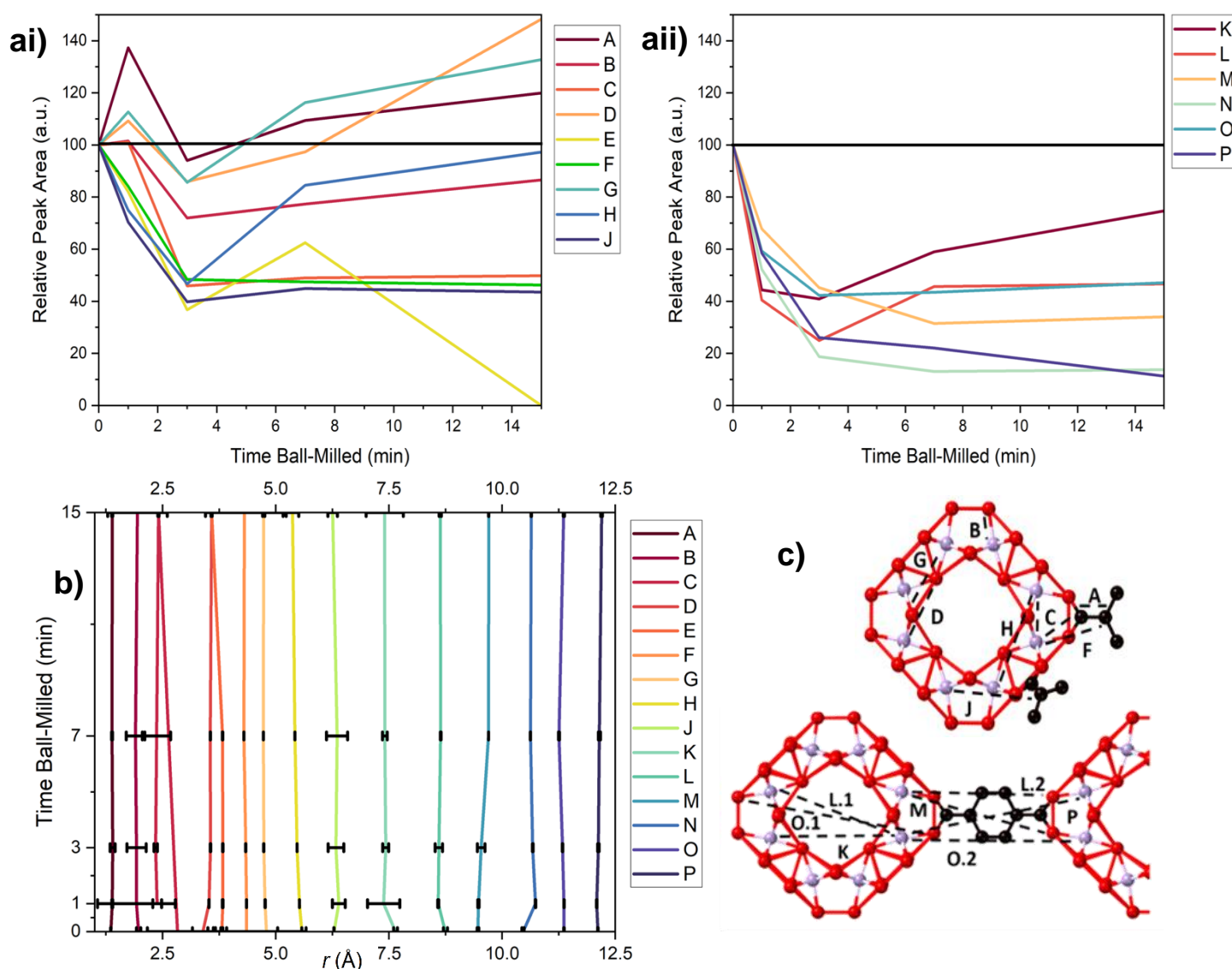


Figure S12: a) Relative peak area of the correlations extracted from Fig. 3a as a function of milling time for: i) peaks with contributions from only the SRO and ii) peaks containing LRO contributions. b) Change in peak position as a function of time ball-milled. The regions highlighted in orange were the most notable peak shifts, resulting in peak overlap. Peak parameters were extracted from PDF spectra using Fityk, with the errors determined from standard deviation extracted from the software.¹⁶ c) Key correlations contributing to the peaks identified in Fig. S9. Peak parameters were extracted through fitting equivalent to that in Fig. S11. Peak areas were combined, and peak positions averaged, where contributions were experimentally observed to contribute to one named peak.

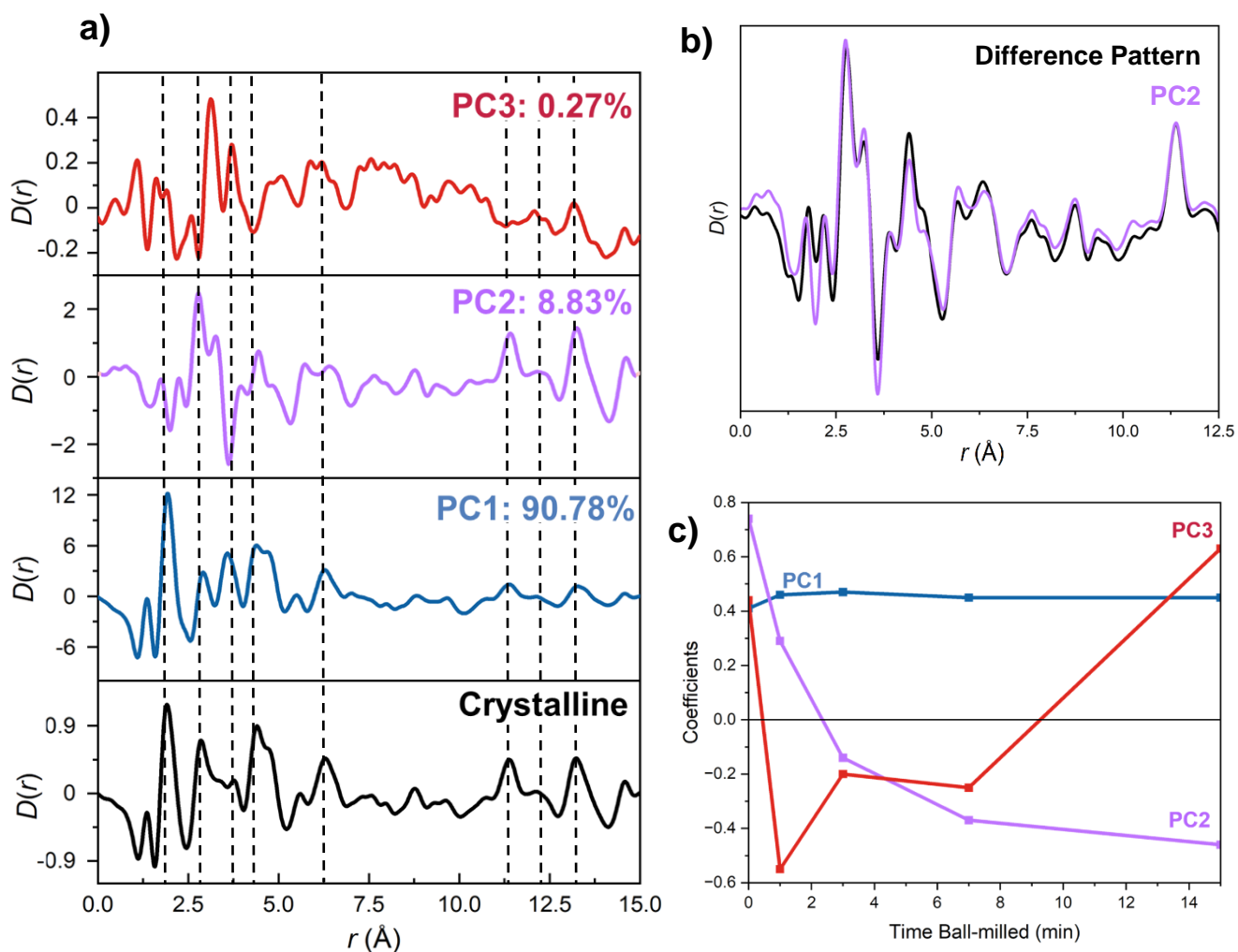


Figure S13: a) Principal component analysis of the composites with % variance values of 90.78, 8.83, and 0.27% for PC1, PC2 and PC3, respectively, with comparison to crystalline MIL-125-NH₂. Eigenvalues were 4.54, 0.44 and 0.013 respectively. b) Comparison of PC2 with the rescaled difference pattern between crystalline and a_m MIL-125-NH₂. c) Coefficients of each principal component as a function of time ball-milled. The low contribution to the variance of PC3 meant it wasn't considered significant for further analysis.

Table S4: Principal component analysis contributions to pair distribution function spectra of ball-milled MIL-125-NH₂.

TIME BALLMILLED (MIN)	COEFFICIENTS		
	PC1	PC2	PC3
0	0.41	0.74	0.44
1	0.46	0.29	-0.55
3	0.47	-0.14	-0.20
7	0.45	-0.37	-0.25
15	0.45	-0.46	0.63

Table S5: Principal component analysis Pearson correlations

TIME BALLMILLED (MIN)	0	1	3	7	15
0	1	0.94228	0.81817	0.71748	0.6805
1	0.94228	1	0.95472	0.89931	0.86657
3	0.81817	0.95472	1	0.98365	0.96957
7	0.71748	0.89931	0.98365	1	0.9918
15	0.6805	0.86657	0.96957	0.9918	1

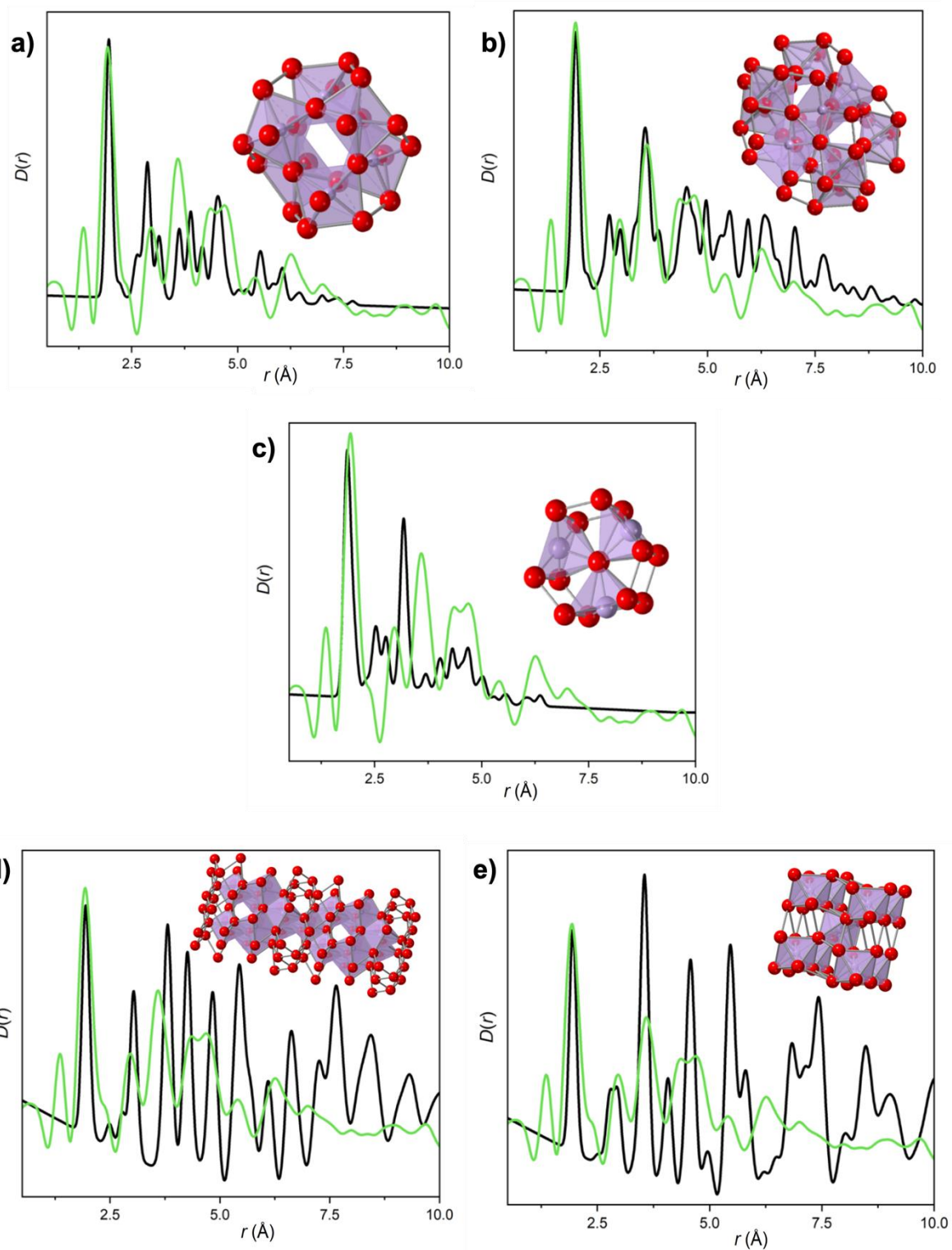


Figure S14: PDFs of simulated SBUs of Ti-MOFs (black) compared to $a_m\text{MIL-125-NH}_2$ (green), insets show structure of these SBUs with Ti (purple) and oxygen (red). a) MOF-901 (Ti_6O_6)¹⁷ b) MIL-177-LT ($\text{Ti}_{12}\text{O}_{15}$)¹⁸, c) COK-69 ($\text{Ti}_3(\mu_3\text{-O})$)¹⁹, equivalent to MIL-100(Ti)²⁰. PDFs of simulated TiO_2 structures (black) compared to $a_m\text{MIL-125-NH}_2$ (green), d) anatase, e) rutile.²¹

5. X-ray Photoelectron Spectroscopy

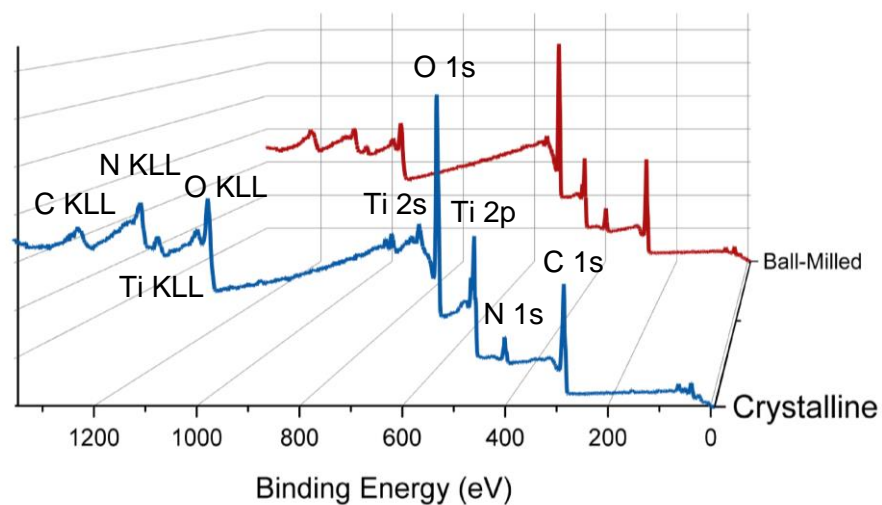


Figure S15: XPS survey of crystalline (blue) and amorphous (red) MIL-125-NH₂.

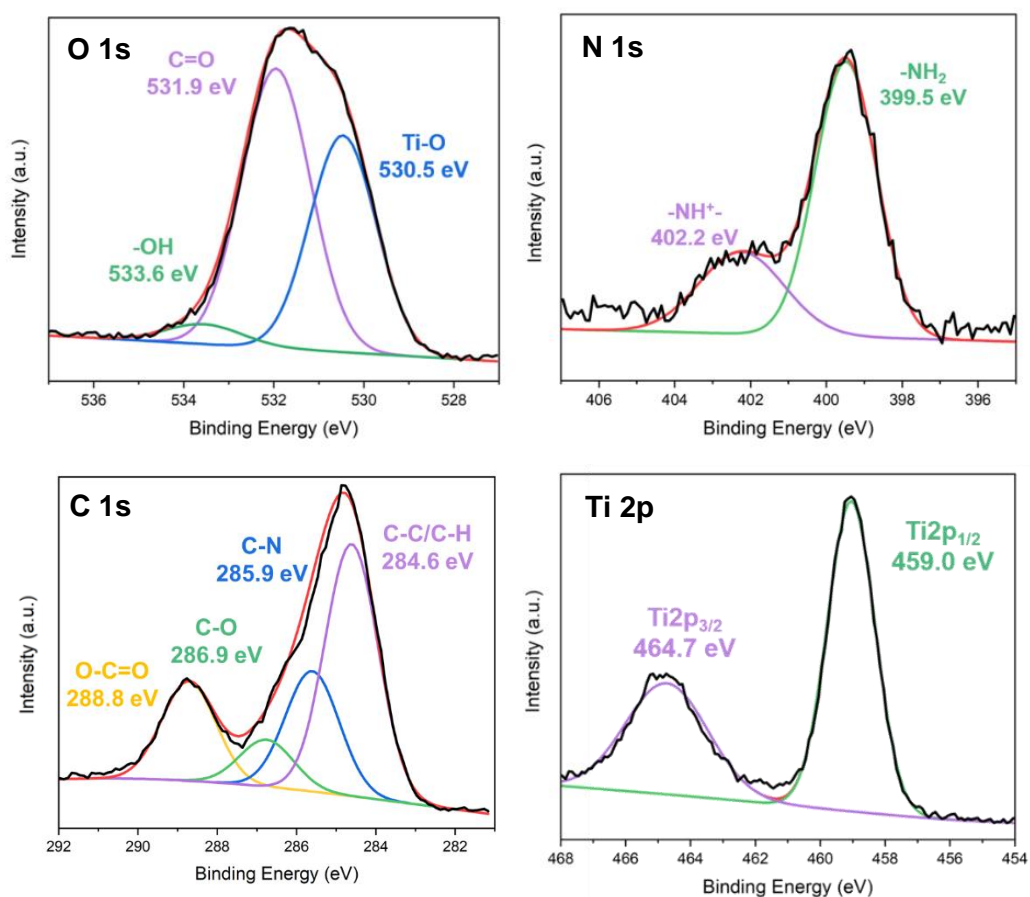


Figure S16: XPS spectra of crystalline MIL-125-NH₂, with deconvoluted contributions labelled.

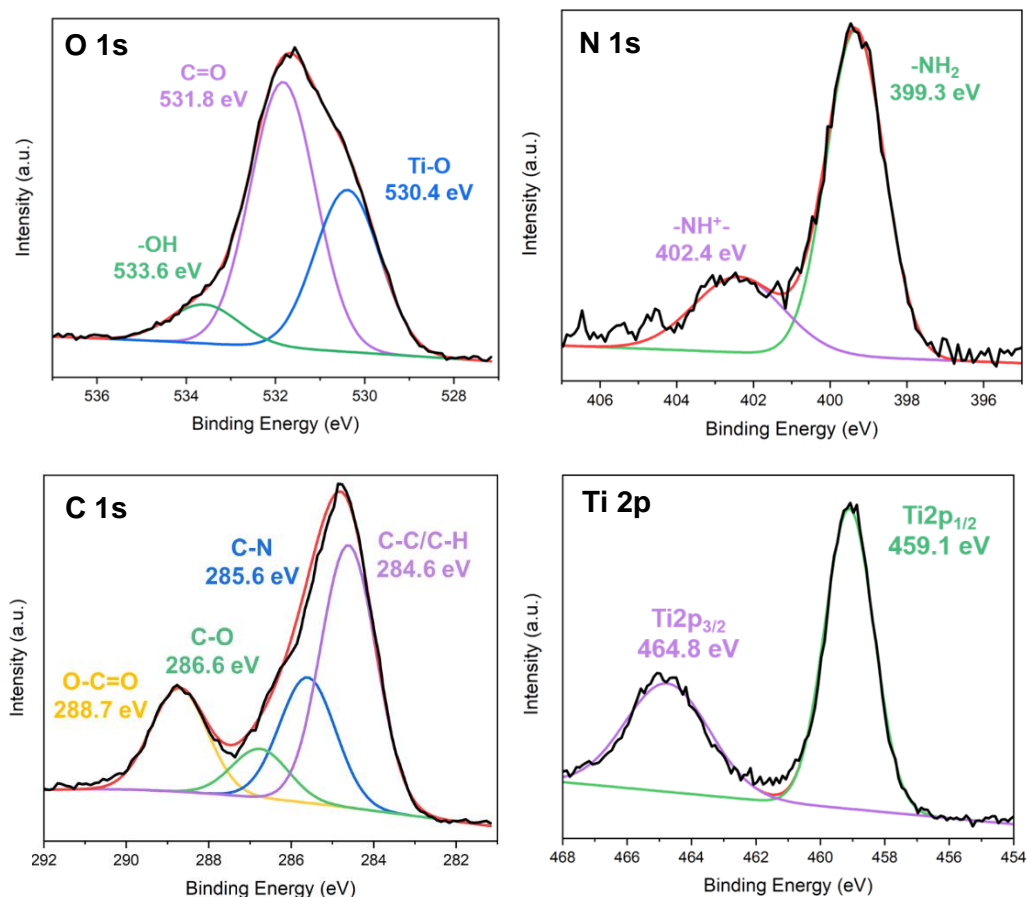


Figure S17: XPS spectra of ball-milled aMIL-125-NH₂, with deconvoluted contributions labelled.

Table S6: Summary of the fittings of the deconvoluted contributions from Figures S14 and S15, extracted using Fityk.¹⁶

	PEAK AREA / a.u.		RELATIVE PEAK AREA*	
	CRYSTALLINE	AMORPHOUS	CRYSTALLINE	AMORPHOUS
Ti-O	14312.4	10697.9	1	1
C=O	18510.5	17527.9	1.3	1.64
OH	1499.83	2741.99	0.1	0.26
NH ⁺	1204.29	1247.03	0.08	0.12
NH ₂	2879.28	3500.54	0.2	0.33
O-C=O	2939.35	3228.81	0.23	0.3
C-O	1356.35	1523.09	0.09	0.14
C-N	2889.29	3898.45	0.2	0.36
C-C/C-H	8456.05	8048.52	0.6	0.75
Ti 2p _(1/2)	8626.9	6458.04	0.6	0.6
Ti 2p _(3/2)	13928.4	10397	0.97	0.97

* Relative peak area compared to Ti-O

6. Fourier-Transform Infrared Spectroscopy

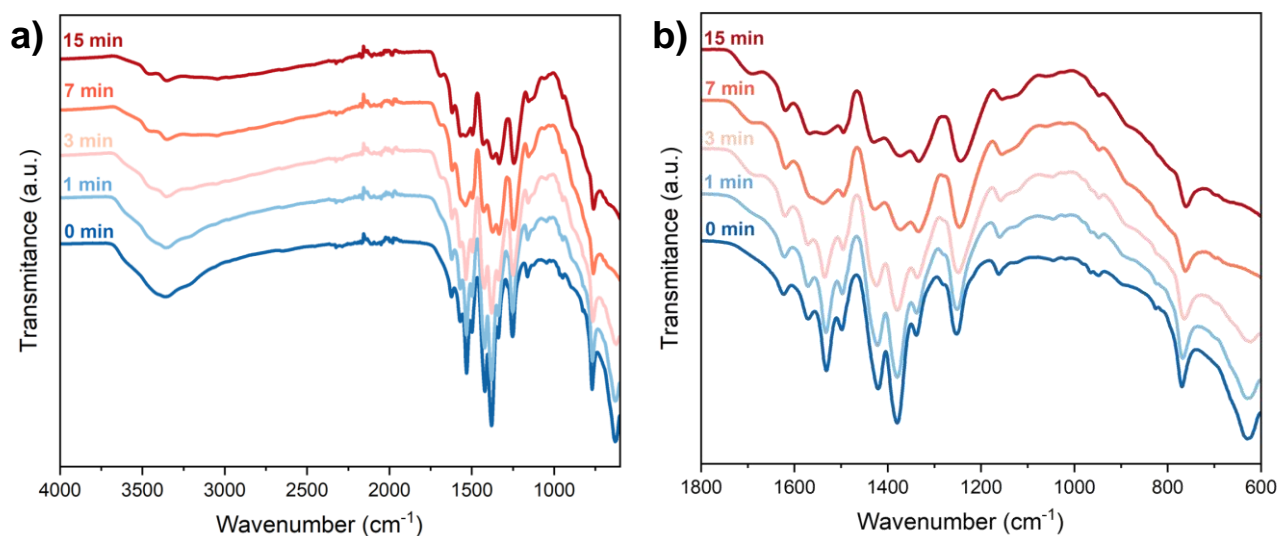


Figure S18: FT-IR spectra of MIL-125-NH₂ with respect to time ball-milled. a) full spectra, b) zoomed in region.

Table S7: Key vibrational assignments of MIL-125-NH₂, from FT-IR spectra, Figure S13b. Extracted using Fityk.¹⁶

	PEAK POSITION / cm ⁻¹		PEAK AREA / a.u.	
	CRYSTALLINE	AMORPHOUS	CRYSTALLINE	AMORPHOUS
NH DEFORMATION	1531	1538	866.905	814.214
CN VIB.	1421	1429	1232.54	389.451
CO VIB. (ASYMMETRIC)	1570, 1498	1567, 1495	453.833, 428.392	833.855**, 257.392
CO VIB. (SYMMETRIC)	1380	1373	1558.44	912.118
UNCOORDINATED CO VIB.	N/A	1689	N/A	454.82
O-TI-O VIB.	400-800	400-800	Broad	Broad

** Contains contribution from monocoordinated CO peak at ~1550 cm⁻¹.

7. Compositional Analysis

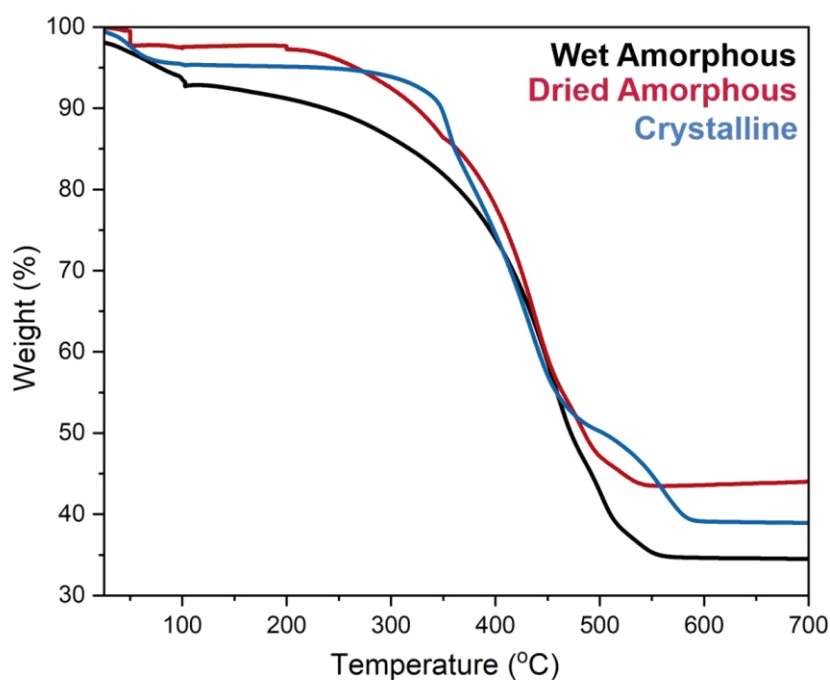


Figure S19: Thermogravimetric data of MIL-125-NH₂ (blue). *a*_mMIL-125-NH₂ samples were also run both on long-term exposure to air (black) and dried prior to analysis (red). Heating was performed under air at 10 °C min⁻¹.

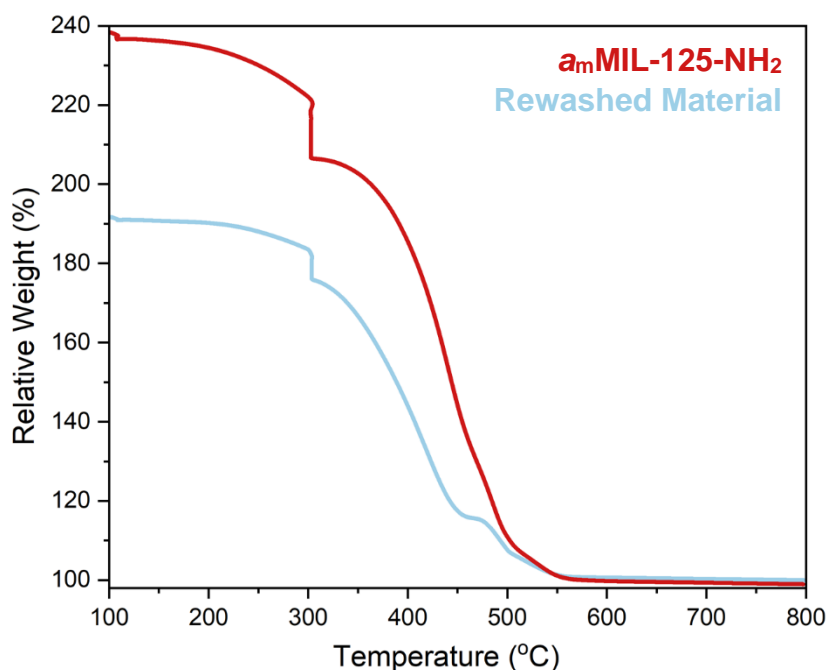


Figure S20: Thermogravimetric data of *a*_mMIL-125-NH₂ (red) and washed *a*_mMIL-125-NH₂ (blue). Heating was performed under air. Isotherms were performed at 100 °C and 300 °C for 10 minutes, with a heating rate of 10 °C min⁻¹. Weight % was rescaled according to the end point.

Table S8: Thermogravimetric analysis data of MIL-125-NH₂, with calculated theoretical compositions. Start and end signify the process of decomposition. Theoretical ideal composition was taken as Ti₈O₈(OH)₄(BDC-NH₂)₆, BDC-NH₂ = C₈O₄H₅N.

	START % WEIGHT	END % WEIGHT	COMPOSITION
MIL-125-NH ₂	94.4	39.2	Ti ₈ O _{8.417} (OH) ₄ (C ₈ O ₄ H ₅ N) _{5.583}
a _m MIL-125-NH ₂	94.0	43.7	Ti ₈ O _{9.01} (OH) ₄ (C ₈ O ₄ H ₅ N) _{4.99}
REWASHED	97.3	51.2	Ti ₈ O _{11.03} (OH) ₄ (C ₈ O ₄ H ₅ N) _{2.97}

Table S9: CHN analysis of the MIL-125-NH₂ materials.

	%C	%H	%N
THEORETICAL	34.86	3.07	5.08
MIL-125-NH ₂	28.36	5.09	4.80
a _m MIL-125-NH ₂	31.63	2.85	5.20
REWASHED	24.96	2.44	4.07

8. Applications

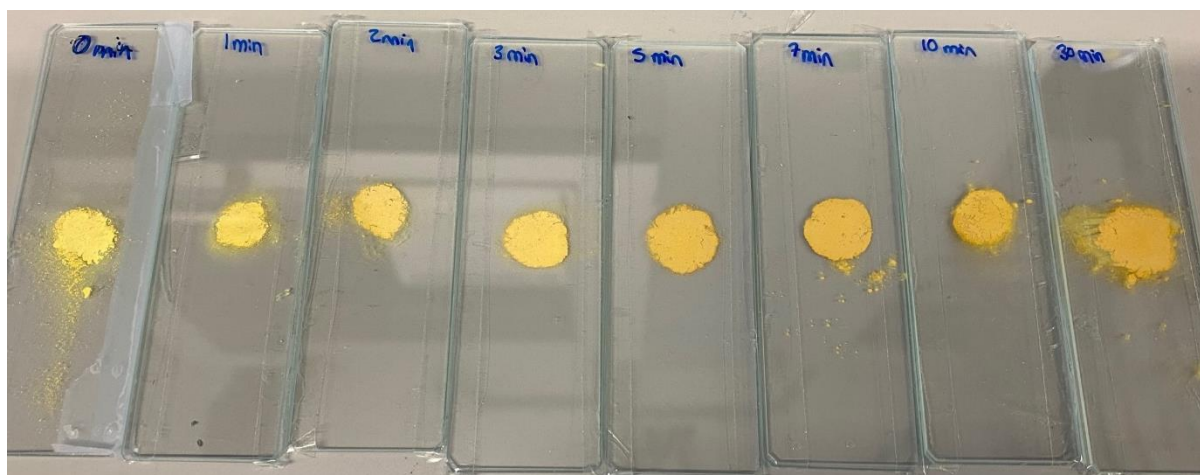


Figure S21: Image of samples of MIL-125-NH₂ ball-milled for varying amounts of time to display the observed colour change. The colour was observed to darken from left to right, as time ball-milling increased.

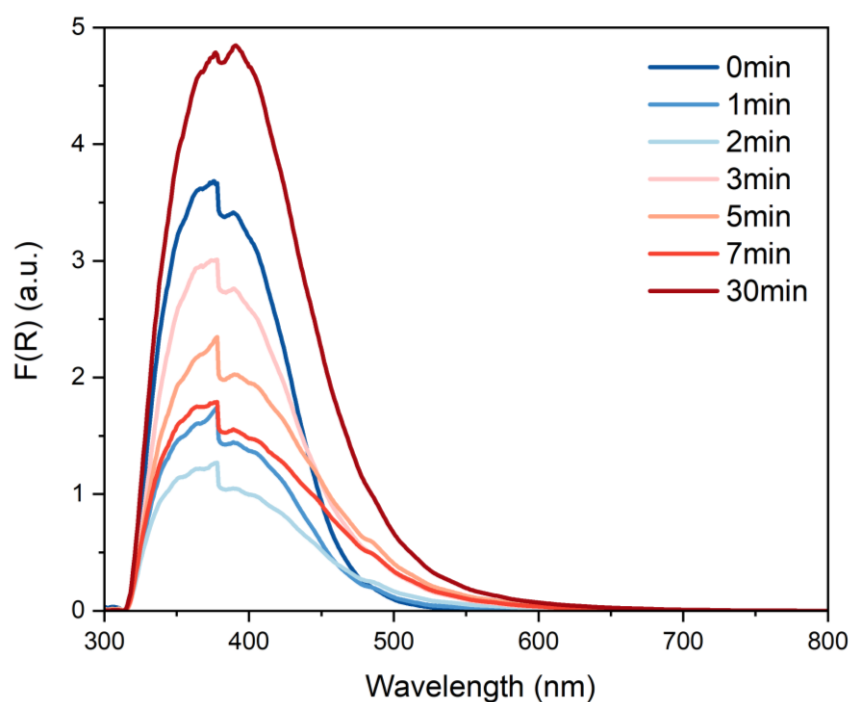


Figure S22: UV-Vis diffuse reflectance spectra. Key shows duration of ball milling in minutes. The feature observed ~400 nm was attributed to a change between detectors.

Scheme S1: Photocatalytic evaluation of materials in the oxidative coupling of amines to imines

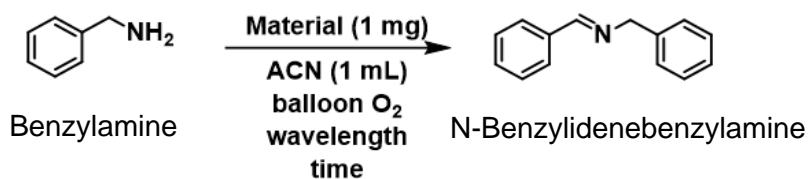


Table S10: Photocatalytic activity testing of MIL-125-NH₂ and *a_m*MIL-125-NH₂ materials.

Entry	Material	Wavelength (nm)	Time (h)	¹ H NMR yield (%)
1	MIL-125-NH ₂	450	24	36
2	<i>a_m</i> MIL-125-NH ₂			20
3	MIL-125-NH ₂	520	48	22
4	<i>a_m</i> MIL-125-NH ₂			11

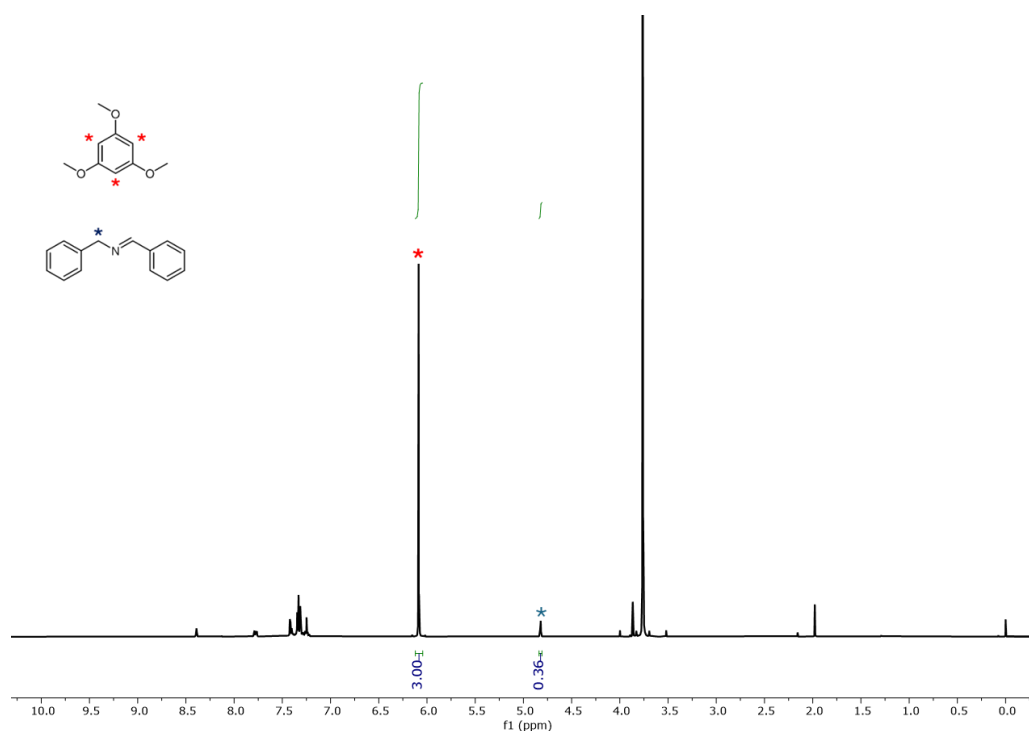
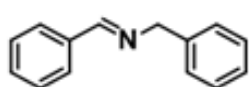


Figure S23: Example of the yield quantification by ¹H NMR using 1,3,5-trimethoxybenzene as internal standard.



¹H NMR (300 MHz, CDCl₃) δ 8.39 (s, 1H), 7.79 (dd, *J* = 6.2, 2.1 Hz, 2H), 7.42 (dd, *J* = 5.6, 2.2 Hz, 3H), 7.34 (d, *J* = 4.5 Hz, 4H), 7.26-7.24 (m, 1H), 4.84 (s, 2H) ppm. Spectra data are consistent with those reported in the literature.²²

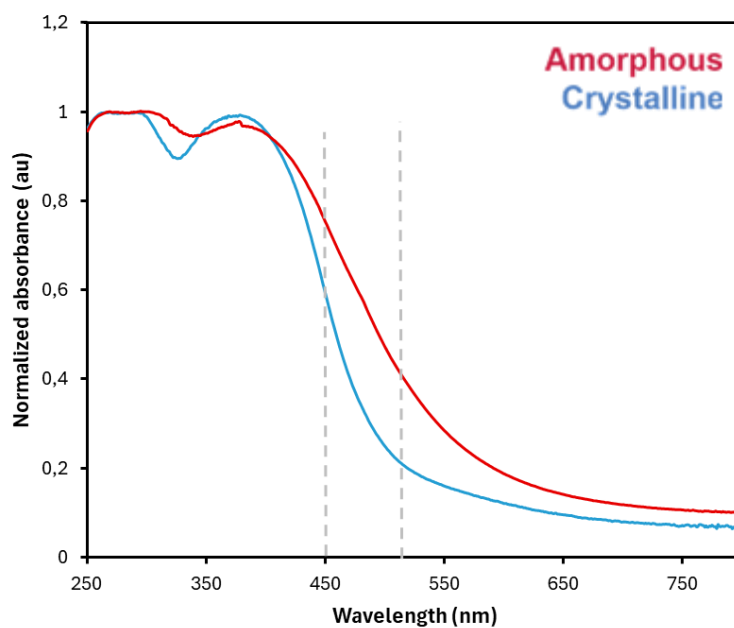


Figure S24: Normalised absorbance of crystalline (blue) and amorphous (red) MIL-125-NH₂. The dashed lines represent the irradiation wavelengths.

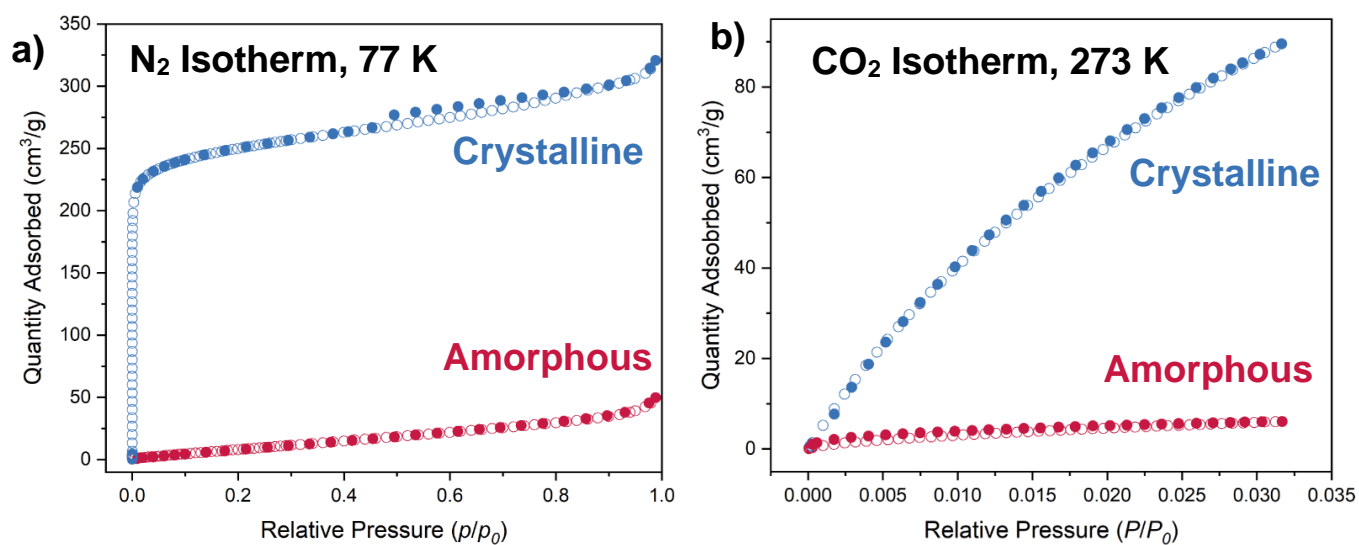


Figure S25: Adsorption (open circles) and desorption (closed circles) isotherms for crystalline (blue) and amorphous (red) MIL-125-NH₂. a) N₂ adsorption/desorption isotherms at 77 K. b) CO₂ adsorption/desorption isotherms collected at 273 K.

9. References

- 1 A. A. Coelho, *J Appl Crystallogr*, 2018, 51, 210–218.
- 2 D. Johnstone, P. Crout, C. Francis, M. Nord, J. Laulainen, S. Høgås, E. Opheim, E. Prestat, B. Martineau, T. Bergh, N. Cautaeerts, H. W. Ånes, S. Smeets, V. J. Femoen, A. Ross, J. Broussard, S. Huang, S. Collins, T. Furnival, D. Jannis, I. Hjorth, E. Jacobsen, M. Danaie, A. Herzing, T. Poon, S. Dagenborg, R. Bjørge, A. Iqbal, J. Morzy, T. Doherty, T. Ostasevicius, T. I. Thorsen, M. von Lany, R. Tovey and P. Vacek, *Zenodo*, 2024, preprint, DOI: 10.5281/zenodo.11585254.
- 3 G. I. Lampronti, A. A. L. Michalchuk, P. P. Mazzeo, A. M. Belenguer, J. K. M. Sanders, A. Bacchi and F. Emmerling, *Nat Commun*, 2021, 12, 6134.
- 4 P. P. Mazzeo, G. I. Lampronti, A. A. L. Michalchuk, A. M. Belenguer, A. Bacchi and F. Emmerling, *Faraday Discuss*, 2023, 241, 289–305.
- 5 C. Ye, G. I. Lampronti, L. N. McHugh, C. Castillo-Blas, A. Kono, C. Chen, G. P. Robertson, L. A. V. Nagle-Cocco, W. Xu, S. D. Stranks, V. Martinez, I. Brekalo, B. Karadeniz, K. Užarević, W. Xue, P. Kolodzeiski, C. Das, P. Chater, D. A. Keen, S. E. Dutton and T. D. Bennett, *Chem Sci*, 2024, 15, 7198–7205.
- 6 D. A. Keen, *Crystallogr Rev*, 2020, 26, 143–201.
- 7 D. A. Keen, *J Appl Crystallogr*, 2001, 34, 172–177.
- 8 A. K. Soper and E. R. Barney, *J Appl Crystallogr*, 2011, 44, 714–726.
- 9 C. L. Farrow, P. Juhas, J. W. Liu, D. Bryndin, E. S. Božin, J. Bloch, T. Proffen and S. J. L. Billinge, *Journal of Physics: Condensed Matter*, 2007, 19, 335219.
- 10 *Origin Lab, USA*, preprint, Origin Lab, USA:2023.
- 11 P. R. Jubu, O. S. Obaseki, D. I. Ajayi, E. Danladi, K. M. Chahrour, A. Muhammad, S. Landi, T. Igbawua, H. F. Chahul and F. K. Yam, *Journal of Optics*, DOI:10.1007/s12596-024-01741-0.
- 12 P. H. M. Andrade, C. Volkringer, T. Loiseau, A. Tejada, M. Hureau and A. Moissette, *Appl Mater Today*, 2024, 37, 102094.
- 13 V. Kavun, E. Uslamin, B. van der Linden, S. Canossa, A. Goryachev, E. E. Bos, J. Garcia Santaclara, G. Smolentsev, E. Repo and M. A. van der Veen, *ACS Appl Mater Interfaces*, 2023, 15, 54590–54601.
- 14 L. Pukdeejorhor, S. Wannapaiboon, J. Berger, K. Rodewald, S. Thongratkaew, S. Impeng, J. Warnan, S. Bureekaew and R. A. Fischer, *J Mater Chem A Mater*, 2023, 11, 9143–9151.
- 15 M. Dan-Hardi, C. Serre, T. Frot, L. Rozes, G. Maurin, C. Sanchez and G. Férey, *J Am Chem Soc*, 2009, 131, 10857–10859.
- 16 M. Wojdyr, *J Appl Crystallogr*, 2010, 43, 1126–1128.
- 17 H. L. Nguyen, F. Gándara, H. Furukawa, T. L. H. Doan, K. E. Cordova and O. M. Yaghi, *J Am Chem Soc*, 2016, 138, 4330–4333.
- 18 S. Wang, T. Kitao, N. Guillou, M. Wahiduzzaman, C. Martineau-Corcoc, F. Nouar, A. Tissot, L. Binet, N. Ramsahye, S. Devautour-Vinot, S. Kitagawa, S. Seki, Y. Tsutsui,

- V. Briois, N. Steunou, G. Maurin, T. Uemura and C. Serre, *Nat Commun*, 2018, 9, 1660.
- 19 B. Bueken, F. Vermoortele, D. E. P. Vanpoucke, H. Reinsch, C. Tsou, P. Valvekens, T. De Baerdemaeker, R. Ameloot, C. E. A. Kirschhock, V. Van Speybroeck, J. M. Mayer and D. De Vos, *Angewandte Chemie International Edition*, 2015, 54, 13912–13917.
- 20 B. Bueken, F. Vermoortele, D. E. P. Vanpoucke, H. Reinsch, C. Tsou, P. Valvekens, T. De Baerdemaeker, R. Ameloot, C. E. A. Kirschhock, V. Van Speybroeck, J. M. Mayer and D. De Vos, *Angewandte Chemie International Edition*, 2015, 54, 13912–13917.
- 21 M. Rezaee, S. M. Mousavi Khoie and K. H. Liu, *CrystEngComm*, 2011, 13, 5055.
- 22 A. Jiménez-Almarza, A. López-Magano, R. Mas-Ballesté and J. Alemán, *ACS Appl Mater Interfaces*, 2022, 14, 16258–16268.